Proceedings of the Institution of Mechanical Engineers, Part B: Journal of Engineering Manufacture

Parametric finite element analysis of stress evolution during friction stir welding

C M Chen and R Kovacevic

The online version of this article can be found at:

Published by:

$SAGE

On behalf of:

Institution of MECHANICAL ENGINEERS

Institution of Mechanical Engineers

Additional services and information for _Proceedings of the Institution of Mechanical Engineers, Part B: Journal of Engineering Manufacture_ can be found at:

Email Alerts: http://pib.sagepub.com/cgi/alerts

Subscriptions: http://pib.sagepub.com/subscriptions

Reprints: http://www.sagepub.com/journalsReprints.nav

Permissions: http://www.sagepub.com/journalsPermissions.nav

Citations: http://pib.sagepub.com/content/220/8/1359.refs.html

>> Version of Record - Aug 1, 2006

What is This?

Parametric finite element analysis of stress evolution during friction stir welding

C M Chen and **R Kovacevic***

Department of Mechanical Engineering, Southern Methodist University, Richardson, Texas, USA

Abstract: It is well known that the residual stress of the friction-stir-welded joint affects the fatigue strength and life, and the corrosion performance. In this paper, a three-dimensional finite element model is established to study the thermal history and stress evolution in the butt welding of aluminium alloy 6061-T6, which will comprehensively provide insight into the friction-stir-welding process. The mechanical action of the shoulder and the thermomechanical effect of the tool (including shoulder and probe) are included in the comprehensive model. The orthogonal stress evolution of the weld is given in this paper. The relationship between the calculated residual stresses of the weld and the process parameters such as the tool traverse and rotational speeds, and the fixture release are investigated and presented.

Keywords: friction stir welding, finite element model, stress evolution, thermomechanical effect, residual stress, aluminium alloy A6061-T6.

1 INTRODUCTION

Friction stir welding (FSW) has been widely used for various materials, primarily for joining aluminium alloys [1–4]. As for the low heat input and pure solid joining for this process, the final weld will be expected to have a low amount of distortion compared with those welds obtained by fusion-welding methods. The residual stress forms as a consequence of the complicated thermomechanical and mechanical processes and adversely affects the fatigue and corrosion performance [5, 6]. A computer analysis of the stress evolution in the weld will be beneficial to obtain insight into the process and thus provide guidelines for designers, especially in the case of complex shape variations.

Some progress has been made in the prediction and measurement of the temperature and residual stress in FSW. Song and Kovacevic [7, 8] have modelled the heat transfer in FSW using the finite difference method. A few papers have directly dealt with the modelling of the thermomechanical stresses in

FSW. Chao and Qi [9] proposed a model to predict the thermal history, and the subsequent thermal stress and distortion of the workpiece without involving the mechanical effect of the tool. Deng, and 10 workers [10, 11] used a solid-mechanics-based finite element model to simulate the plastic flow process in FSW. Dong *et al.* [12] developed several models to deal separately with the subproblems of heat transfer, material flow, and plastic flow. Chen and Kovacevic [13, 14] predicted and measured the temperature, residual stresses, and forces during FSW. Ulysse [15] used a three-dimensional model to simulate the tool force in FSW. Shi *et al.* [16, 17] conducted thermomechanical modelling of FSW including tool loads. However, little work has been reported on the parametric investigation of FSW.

In this paper, the effect of traverse and rotational speeds, and the fixture release on the stress evolution of the weld were investigated on the basis of a three-dimensional model by considering the mechanical effect of the tool. The simulation is implemented using the commercial finite element package ANSYS. Experiments on the welding of aluminium alloy 6061-T6 are also carried out. The temperature history and the orthogonal stress evolution for the welded plates are simulated and represented.

Corresponding author: Department of Mechanical Engineering, Southern Methodist University, Research Centre for Advanced Manufacturing, 1500 International Parkway, Suite no. 100, Richardson TX 75081, USA. email: kovacevi@engr.smu.edu

2 MODEL DESCRIPTION

The welding process is shown in Fig. 1, where V is the traverse speed of the tool and ω is its rotational speed. The tool is made of CPM3V and consists of the shoulder and probe, with diameters of $R_0 = 24$ mm and $r_0 = 6$ mm respectively. The welded plates are aluminium alloy 6061-T6, and each has a rectangular shape with a size of 240 mm × 50 mm × 6 mm. Rotational speeds of 344 and 500 r/min and traverse speeds of 140 and 350 m/s are selected for this investigation because the use of these parameters produces good-quality welds with a sound microstructure. The tool is considered a rigid solid, and the workpiece is considered a ductile material characterized with elasticity, plasticity, and a kinetic hardening effect. The properties of AISI A2 steel and aluminium alloy 6061-T6 are given in Table 1 [9].

2.1 Heat transfer model

The temperature calculation is based on the heat conduction equation

$$\rho c \frac{\mathrm{d}T}{\mathrm{d}t} = \mathrm{div}(k \operatorname{grad} T) + q \tag{1}$$

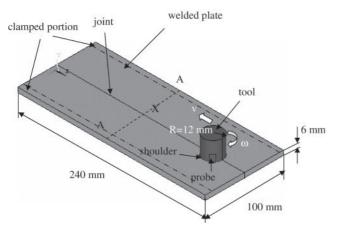where q is the power generated by the friction between the tool and the top of the workpiece, and

Fig. 1 A schematic illustration of the FSW process

by the plastic deformation work of the central weld zone, T is the temperature, k is the conductivity, ρ is the material density, and c is the heat capacity.

The main heat source in FSW is generally considered to be the friction between the rotating tool and the welded plates, and the 'cold work' in the plastic deformation of material in the vicinity of the tool. Considering an element at the contact surface between the tool shoulder and the top surface of workpiece, the rate of heat generation derived from the friction in the element at radius r is

$$\mathrm{d}\dot{q} = 2\pi\omega r^2 \mu(T)p(T)\,\mathrm{d}r \tag{2}$$

The rate of heat generation (caused by the friction) over the entire interface of the contact will be

$$\dot{q} = \int_{r_0}^{R_0} 2\pi\omega r^2 \mu(T)p(T)\,\mathrm{d}r = \tfrac{2}{3}\pi\omega\mu(T)p(T)\left(R_0^3 - r_0^3\right) \tag{3}$$

The rate of heat generation at the interface between the shoulder and the top of the workpiece surface is a function of the friction coefficient $\mu(T)$, angular velocity ω, and radius r. Since $\mu(T)$ and $p(T)$ are dependent on the local temperature and the radius r, equation (3) is difficult to evaluate. As the temperature increases, the friction coefficient is expected to decrease, and the work of the plastic deformation increases. In this model, p is found from the experimental measurement. A constant value of 0.3, which is based on the calculation from the torque curve, is used as the friction coefficient to approximate the comprehensive effect of both factors of the thermal and plastic effects during FSW. The heat generation in the vicinity of the probe is considered the same as that at the shoulder periphery with a radius equal to that of the probe.

The top and bottom surfaces of the welded plate are assumed to have two different heat transfer coefficients. The radiation of the surfaces is believed to be small during FSW, and the heat transfer due to the radiation is included in the convection. The heat convection coefficient 38 W/m^2 °C is used for the top surface. At the bottom surface of the plate, the

Table 1 Material properties of AISI A2 Steel and aluminium alloy 6061-T6 [9]

	Temperature (°C)	Thermal conductivity (W/m °C)	Heat capacity (J/kg °C)	Density (kg/m^3)	Young's modulus (GPa)	Yield strength (MPa)	Thermal expansion (μ/°C)	Poisson's ratio	Melting point (°C)
AISI A2 steel		23.8	500	7860	203		10.6	0.29	
Aluminium alloy 6061-T6	0	162	917	2703	69.7	277.7	22.4	0.23	582–652
	93.3	177	978	2685	66.2	264.6	24.61		
	204.4	192	1028	2657	59.2	218.6	26.6		
	315.6	207	1078	2630	47.78	66.2	27.6		
	427.7	223	1133	2602	31.72	7.9	29.6		
	571.1	253	1230	2574	0	0	34.2		

contact conduction resistance is anticipated for the heat flow. The heat convection coefficient $200 \, \text{W/m}^2 \, ^\circ\text{C}$ is used for the bottom surface to account for the heat flowing to the backing plate. Symmetry is assumed along the centre-line of the welded plate.

2.2 Mechanical model

The force equilibrium on an arbitrary volume results in a governing equation which is known as the equilibrium equation and is given by

$$\text{div}(\boldsymbol{S}) + F = \rho\gamma \tag{4}$$

where $\boldsymbol{S}$ is the stress tensor, ρ is the equivalent density, γ is the acceleration, and F is the volume force intensity. The inertial effect is neglected in this model since a constant rotational speed and a constant longitudinal speed are used during FSW.

The stress formed in the weld is a result of the thermal gradient, elastic deformation, and plastic deformation of the material. The stress–strain equation is described as

$$\boldsymbol{S} = [M]\boldsymbol{\varepsilon} \tag{5}$$

where $\boldsymbol{\varepsilon}$ is the total strain tensor and $[M]$ is the stress function matrix. The total strain tensor $\boldsymbol{\varepsilon}$ can be decomposed as

$$\boldsymbol{\varepsilon} = \boldsymbol{\varepsilon}^{\text{e}} + \boldsymbol{\varepsilon}^{\text{p}} + \boldsymbol{\varepsilon}^{\text{t}} \tag{6}$$

where $\boldsymbol{\varepsilon}^{\text{e}}$ is the elastic part, $\boldsymbol{\varepsilon}^{\text{p}}$ is the plastic part, and $\boldsymbol{\varepsilon}^{\text{t}}$ is the thermal part.

The thermal strain can be computed by the equation

$$\boldsymbol{\varepsilon}^{\text{t}} = [B]\Delta T \tag{7}$$

where $[B]$ is the strain function matrix and ΔT is the difference between the current and reference temperatures.

Displacement is given by

$$U = [D]\boldsymbol{\varepsilon} \tag{8}$$

where $[D]$ is the displacement function matrix.

In the displacement formulation, the essential boundary conditions are specified as

$$U = 0 \tag{9}$$

for the clamped portion of the plate surface and the normal displacement

$$U_y = 0 \tag{10}$$

for the bottom of the plate at y = 0. A free boundary condition is applied to the symmetry plane before the welding.

2.3 Finite element model

ANSYS is commercial finite element method software, which was used to carry out the numerical simulation. In the simulation, the thermomechanically coupled three-dimensional Lagrangian finite element model incorporating temperature and multi-linear strain-hardening effects is used for the three-dimensional modelling of the solid structures. The element topology used is eight nodes and has plasticity, stress stiffening, large deflection, and large-strain capabilities [18].

Symmetry along the weld line is assumed in the calculation; so, one half of the welded plate is meshed with a total of 3537 nodes. In modelling the temperature history, the moving heat sources of the shoulder and the probe are represented as moving the heat generation of the nodes in each computational time step. The mechanical effect by the shoulder is involved in the mechanical model, as the relatively larger contact region of the shoulder and the workpiece is expected to contribute a large part of the mechanical stress, especially in the top part of the weld.

The temperature gradient is large around the welding zone and seriously changes the material's properties. In order to increase the accuracy of the mechanical solution, the thermal and mechanical solutions are coupled; the temperature data at each increment time are used to evaluate the mechanical properties and the thermal parameters.

3 EXPERIMENT SET-UP

Two plates are butt welded in the adapted vertical milling machine for FSW. In the experiments, eight thermocouples are embedded in one plate, of which four are located 1.6 mm below the top surface, and the other four are located 1.6 mm from the bottom surface, with distances of 10 mm, 14 mm, 22 mm, and 30 mm respectively, to the weld centre-line. The space of the thermocouples in the longitudinal direction is 10 mm. A sensor based on a micrometer measurement unit is used to monitor the plunge depth of the tool. Temperatures are acquired and recorded in a time duration of 0.1 s by a Labview-programmed acquisition system.

4 RESULTS AND DISCUSSION

4.1 Typical microstructure of the weld obtained by FSW

The microstructure of the weld is a result of the thermal history and the plastic deformation of the weld region, and it also affects the residual stress distribution. Figure 2 shows a typical optical micrograph taken from the metallographically prepared specimen. The micrograph reveals four distinct regions: the stirred weld zone (or weld nugget); the thermomechanically affected zone (TMAZ); the
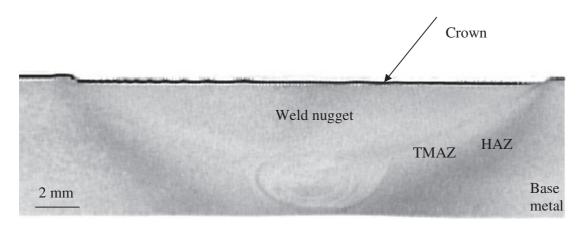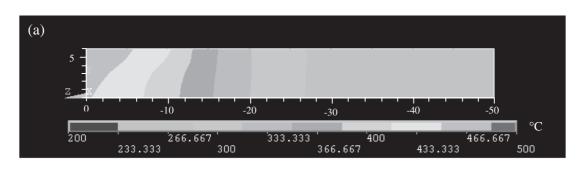
Fig. 2 Typical microstructure of the weld in the cross-section perpendicular to the welding direction
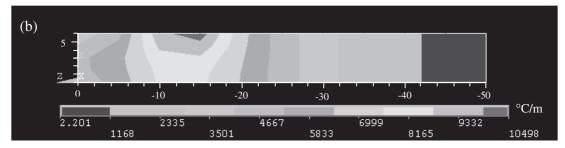

Fig. 3 (a) Temperature contour and (b) temperature gradient (z-direction) contour in the A–A cross-section perpendicular to the weld direction at the moment that the tool moves to the middle point of the plate ($V = 140$ mm/min; $\omega = 500$ r/min)

heat-affected zone (HAZ); the base metal. In the nugget region, the refined grains are equiaxed and are attributed to dynamic recrystallization as a result of the heat and mechanical work. The HAZ usually contains a large amount of coarsened grains with relatively lower yield strength than that in the TMAZ and the nugget, which is believed to be the weakest place for the crack initiation in the tests of fatigue performance and tensile strength.

4.2 Study of temperature–time history in FSW

Figure 3 shows the temperature and temperature gradient contours in the cross-section perpendicular to the welding direction. The highest temperature is observed in the centre of the weld region, extending down from the crown surface to the probe root side, since the rotation of the shoulder and probe contributes the highest heat flux in this region. The relatively higher heat dissipation through the contact surface between the welded plate and the backing plate in comparison with the top surface of the plate causes the temperature contour in the weld nugget area to follow a V shape. Figure 3(b) shows that the maximum temperature gradient in the lateral direction (z direction) arises in the region formed by the edge of the shoulder. This event is attributed to the fact that the highest heat generation in this region and the highest heat radiation dissipation of the region occur just beyond the shoulder edge. The temperature and temperature gradient contours in the lateral direction for the top surface during welding are revealed in

Fig. 3, which proves that the region in contact with the periphery edge of the shoulder is subjected to the highest thermal impact effect. It is believed that the described 'V-type' distribution of the temperature in the weld zone contributes to the grain coarsening in the TMAZ and the HAZ shown in Fig. 2.

4.3 Analysis of the process parameter effect on the stress distribution in the weld

4.3.1 The effect of the traverse and rotational speeds

Stress forms in the weld during the welding owing to the expansion of material that occurs during heating of the welded plates, followed by contraction during cooling of the welds. Furthermore, the rotational and the transverse movements of the tool cause additional stress in the weld due to the mechanical constraint of the plates by the fixture.
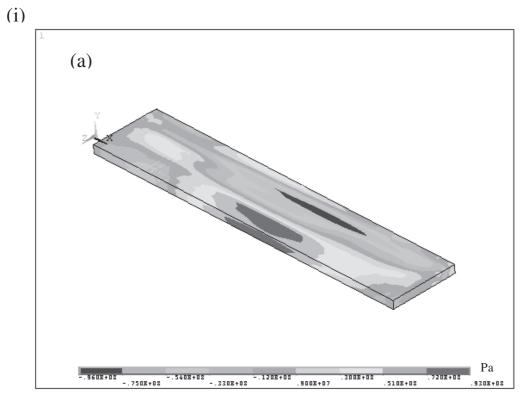
Figure 4 shows the residual stress contours in the longitudinal and lateral directions of the weld. The longitudinal stress (S_x) contour (Figs 4(ia), (iia), and (iiia)) and lateral stress (S_z) contour (Figs 4(ib), (iib), and (iiib)) show that the predicted maximum stress is located in the middle of the weld length. The predicted stress distribution in Fig. 4 is like that encountered in steel welds [19] and also complies with measurements on friction stir-welded aluminium alloy 2024-T3 with the cut compliance method reported by Dalle Donne et al. [5]. It is observed that the start portion and end portion of the weld have different stress distributions in comparison with the middle portion of the plate, which may be caused by the variance in the correlated thermomechanical process during the welding. At the end portion of the weld, the lift-up of the tool leaves the keyhole region in a compressive stress state, as shown in Fig. 4. Both simulation and experiments show that there is little variation in the through-thickness stress S_y [13].

The rotational and travel speeds have a significant effect on the residual stress distribution, as shown in Fig. 4. A lower rotational speed will have a lower heat input into the weld zone, which results in more resistance to the tool movement. Among the three investigated cases, case 1, with a rotational speed of 344 r/min and a traverse speed of 140 mm/min, shows the maximum longitudinal residual stress S_x and lateral residual stress S_z. At the same rotational speed, a higher welding speed induces a larger longitudinal stress over a larger area in the middle portion of the weld, as shown in Figs 4(iia) and (iiia).

Figure 5 shows the longitudinal residual stress in the longitudinal direction (x direction) and the lateral direction (z direction) in the A–A cross-section in the middle portion of the weld with three combinations of rotational and traverse speeds respectively. The longitudinal stress (Figs 5(i)) reveals a maximum value in the region extending down from the crown surface in the weld nugget and tapers throughout the thickness to the bottom surface of the plate. In case 1 (344 r/min; 140 mm/min), in the top half of the weld region, S_x and S_z are tensile stresses and taper significantly beyond the edge of the shoulder along the lateral direction. These simulated results comply with the strain maps of the friction stir weld obtained with the synchrotron X-ray diffraction technique [20]. It is noticeable that the higher tool traverse speed results in a larger high longitudinal stress region (Figs 5(ib) and 5(ic)) and a narrower high lateral stress region (Figs 5(iib) and (iic)) extending down from the crown surface. A lower tool rotational speed induces a larger longitudinal and lateral stress in the clamping and weld zones, as shown in Figs 5(ia) and 5(iia).

From the above description, it is clear that the locations of the high gradient in the residual stresses in both the longitudinal and the lateral directions are in the proximity of the shoulder diameter (12 mm from the centre-line), which is believed to be caused by the high temperature gradient (see Fig. 3(b)) and the high shear force by the shoulder peripherial edge in this region. The sharp changes in temperature and down force at the edge of the shoulder also contribute to the sharp gradient in microstructure, as observed in Fig. 2. The higher tool traverse speed will induce a lower heat input to the weld zone and will result in a larger high-stress zone with a higher stress value in the weld, because the relatively harder metal in the weld zone causes a larger resistance to the plastic extrusion.

Figure 6 shows the three orthogonal stress distributions along the line A–A (as indicated in Fig. 1) on the top surface of the plate. In Fig 6(a), it is demonstrated that the decrease in the rotational speed from 500 to 344 r/min at the traverse speed of 140 mm/min increases the longitudinal residual stress with a more significant effect in the clamping region. The lateral residual stress significantly increases while the rotational speed decreases, as shown in Fig. 6(b). At the same rotational speed, the increase in the traverse speed increases the longitudinal residual stress and decreases the lateral residual stress in the weld zone. Figure 6 also shows that the higher traverse speed induces an increase in the longitudinal stress from 74.3 to 87 MPa and a decrease in the lateral stress from 50 to 42 MPa. The reason for the increase in the longitudinal stress at the higher traverse speed is that the welded material exerts more resistance to the tool movement in the longitudinal direction as a result of the lower
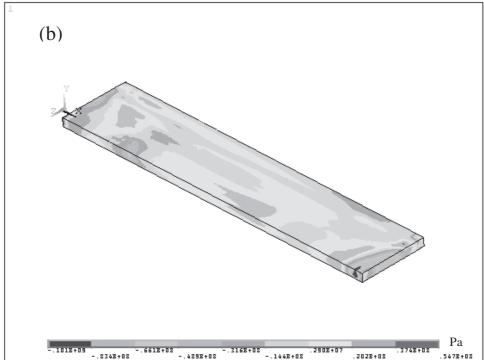
(i)

Fig. 4 Predicted residual stress contour in the welded plate with welding parameters of (i) 344 r/min and 140 mm/min, (ii) 500 r/min and 140 mm/min, and (iii) 500 r/min and 350 mm/min: (a) S_x; (b) S_z

heat input rate. A similar observation for the residual stress measurement of aluminium alloy 6061-T6 by neutron diffraction was also reported by Wang *et al.* [**21**].

4.3.2 The effect of the fixture release

Figure 7 shows how the fixture release affects the stress distribution in the weld at 500 r/min and
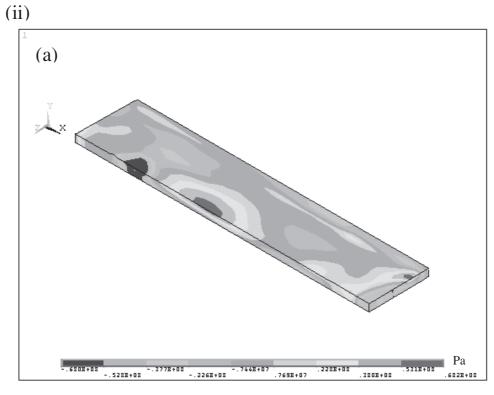
(ii)

Pa

Pa

Fig. 4 (Continued)

140 mm/min. Before the fixture is released, the lateral stress (maximum value of 316 MPa) has higher values than the longitudinal stress (maximum value of 139 MPa), both of which reveal tensile values. After the fixture is released, both S_x (maximum value of 74.3 MPa) and S_z (maximum value of 50 MPa) decrease significantly, and S_x has higher values

than S_z along the lateral direction to not far beyond the edge of the shoulder. In the range between 20 and 45 mm from the centre-line, the longitudinal stress has compressive values. Figure 8 shows the predicted orthogonal stress contour on the A–A cross-section of the welded plate before and after the fixture release. Similar residual stress
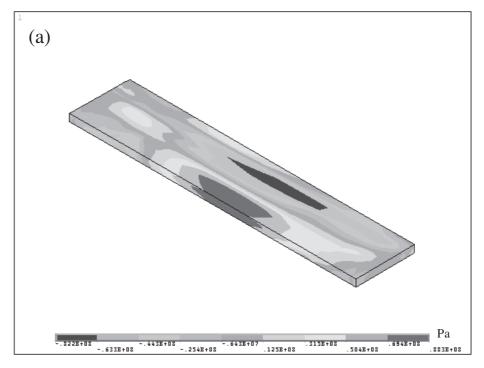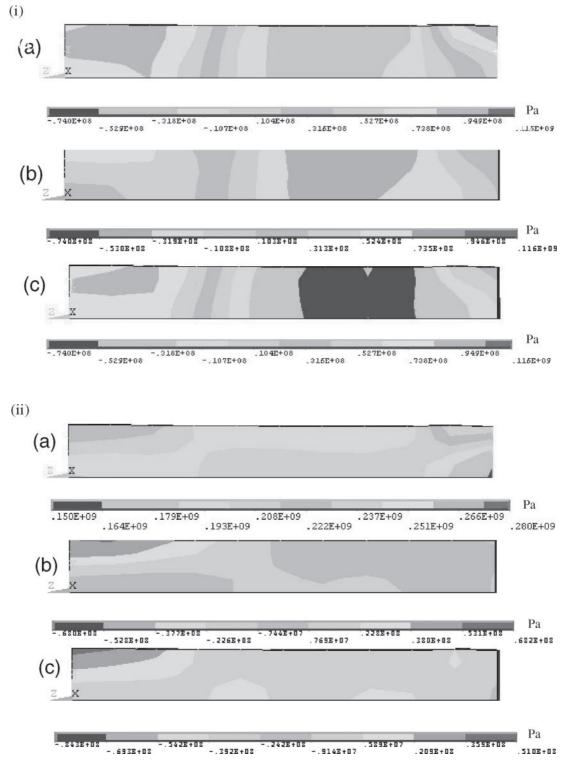
(iii)

Fig. 4   (Continued)

distribution was observed in the friction-stir-welded 7xxx series aluminium alloys [22].

In order to provide a quantitative framework for understanding the dynamics of the thermomechanical properties of FSW, the predicted nodal stress evolution for the node located at the X position (10 mm from the centre-line, shown in Fig. 1) is plotted in Fig. 9. It is revealed that the compressive stresses are formed in both the longitudinal and the lateral directions in front of the tool and decrease as the tool moves near to the node position. It is interesting to note that S_x changes from compressive values to tensile values (maximum of 25.3 MPa) when the tool moves to approximately from 15 to 4 mm behind the node location and then changes again to compressive values (maximum of 33.4 MPa)

Fig. 5 Predicted (i) longitudinal and (ii) lateral residual stress contours on the A–A cross-section of the welded plate at various welding parameters: (a) 344 r/min and 140 mm/min; (b) 500 r/min and 140 mm/min; (c) 500 r/min and 350 mm/min

again approximately 20 mm in front of the node location. Similarly, S_z changes from compressive values to tensile values (maximum of 8 MPa) when the tool moves to approximately from 11 to 6 mm behind the node location and then changes

again to compressive values (maximum of 55.4 MPa) approximately 14 mm in front of the node location.

The vertical stress component S_z has tensile values until the tool moves near the node location, beyond
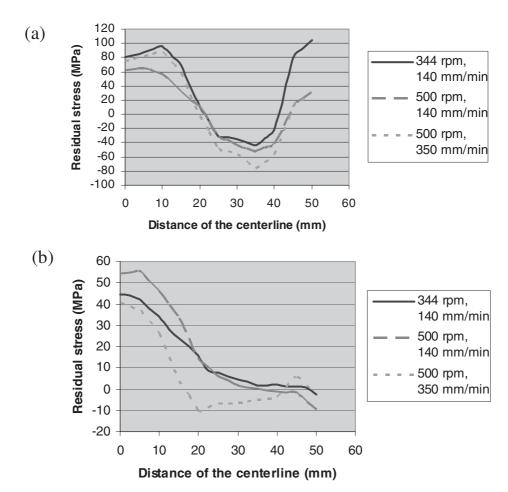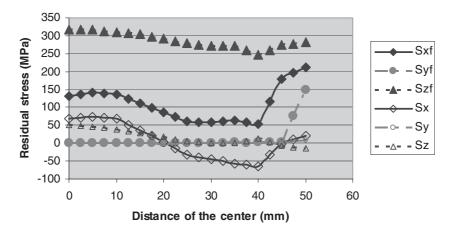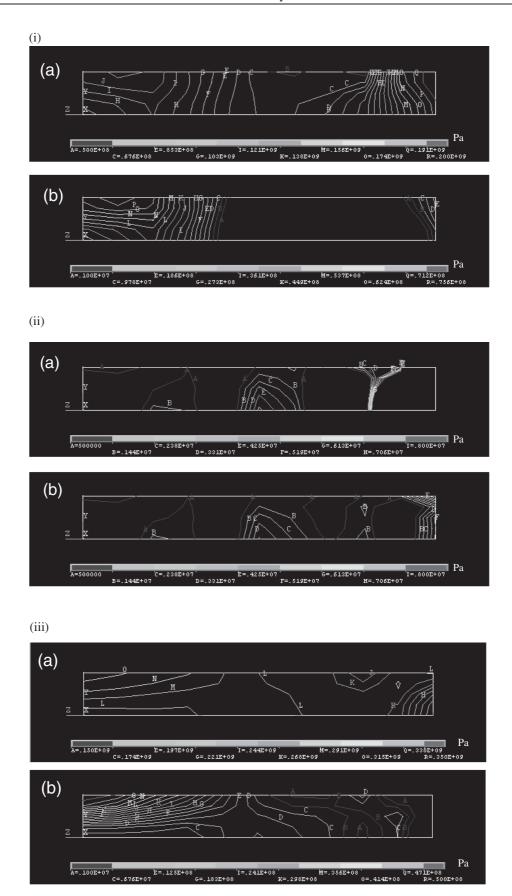
(a)

(b)

Fig. 6 Predicted residual stress distribution along the A–A in the top surface of the plate shown in Fig. 1 with various welding parameters: (a) x direction; (b) z direction

Fig. 7 Predicted orthogonal stress distributions along the line A–A in the top surface of the plate shown in Fig. 1 (500 r/min; 140 mm/min). S_{xf}, S_{yf}, and S_{zf} represent the stress components before the fixture release; S_x, S_y, and S_z represent the residual stress components

which it shows compressive values. Obviously, when the tool moves to a specific range of distance from the node location (approximately from 11 to 6 mm in this case), all three stress components have tensile values, and it is speculated that the most probable welding defects will occur in this region.

Figure 9 also shows that the lateral stress S_z is generally larger than the longitudinal stress S_x S_z during the welding before the fixture is released. In the later welding stage after the tool travels over the node location, the lateral stress for the node X reveals tensile values and increases with time before the fixture

(i)

(ii)

(iii)

Fig. 8 Stress contours of (i) S_x, (ii) S_y, and (iii) S_z in the A–A cross-section (500 r/min; 140 mm/min): (a) before release of the fixture; (b) after release of the fixture
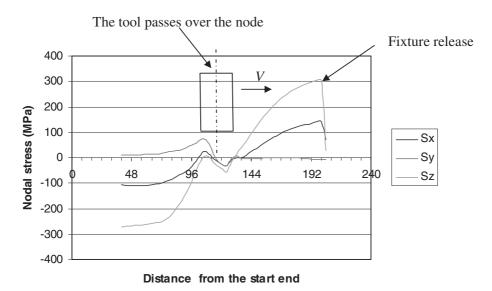
Fig. 9 Predicted nodal stress (S_x, S_y, and S_z) evolution for position X (10 mm from the centre-line) during the FSW (500 r/min; 140 mm/min)

is released, because the increased contraction of the weld as a result of the cooling is restrained by the fixture. A release of the fixture induces significant decreases in both the lateral and the longitudinal stresses, with S_z less than S_x. From this point, controlling the fixture condition during welding and post-welding can be potentially employed to control the residual stresses and deformation, and to prevent cracking in the weld.

5 CONCLUSIONS

A parametric investigation of the effect of rotational, travel speeds, and fixture release on the stress evolution of the weld is performed on the basis of a proposed three-dimensional thermomechanical model including the mechanical action of the shoulder and the thermomechanical effect of the welded material. Modelling of the temperature and stress evolution in the FSW of aluminium alloy 6061-T6 is conducted, with the simulation results validated by the previously conducted measurements.

The prediction and measurement show that the maximum temperature gradients in the longitudinal and lateral directions are located just beyond the shoulder edge. The welding parameter affects the residual stresses significantly. A lower rotational speed increases the lateral and longitudinal residual stresses, especially in the weld and clamping zones. A higher traverse speed increases the longitudinal residual stress in the weld zone but decreases the lateral residual stress. Among the three investigated cases, 500 r/min and 140 mm/min are regarded as the optimum parameters in terms of the lowest resi-

dual stress in the final weld. A higher traverse speed induces a larger longitudinal high-stress zone and a narrower lateral high-stress zone in the weld, which complies with the previously reported results measured with the synchrotron and neutron techniques. Moreover, the prediction reveals that the release of the welded plates from the fixture will affect the stress distribution of the weld significantly. This simulation result demonstrates that, without performing experiments, the modelling technique could potentially be used for the optimization of the FSW process.

REFERENCES

1 **Lienert, T. J., Stellwag, W. L., Grimmentt Jr, B. B.,** and **Warke, R. W**. Friction stir welding studies on mild steel. *Weld. J. Suppl.*, 2003, **82**, 1S–9S.
2 **Reynolds, A. P., Tang, W., Gnaupel-Herold, T.,** and **Prask, H.** Structure, properties, and residual stress of 304L stainless steel friction stir welds. *Scripta Materialia*, 2003, **48**, 1289–1294.
3 **Jata, K. V.** Friction stir welding of high strength aluminum alloys. *Mater. Sci. Forum*, 2000, **331–337**, 1701–1712.

4 **Jata, K. V., Sankaran, K. K.,** and **Ruschau, J. J.** Friction-stir welding effects on microstructure and fatigue of aluminum alloy 7050-T7451. *Metall. Mater. Trans. A*, 2003, **1**, 2181–2193.

5 **Dalle Donne, C., Biallas, G., Ghidini, T.,** and **Raimbeaux, G.** Effect of welding imperfections and residual stresses on the fatigue crack propagation in friction stir welded joints. In Proceedings of the Second International Symposium on *Friction stir welding*, Gothenburg, Sweden, 26–28 June 2000 (TWI, Cambridge).

6 **Zucchi, F., Trabanelli, G.,** and **Grassi, V.** Pitting and stress corrosion cracking resistance of friction stir welded AA 5083. *Mater. Corros.*, 2001, **52**(11), 853–859.

7 **Song, M.** and **Kovacevic, R.** Thermal modeling of friction stir welding in a moving coordinate and its validation. *Int. J. Mach. Tool Mfg*, 2003, **43**(6), 605–615.

8 **Song, M.** and **Kovacevic, R.** Numerical simulation and experimental analysis of heat transfer process in friction stir welding process. *Proc. Instn Mech. Engrs, Part B: J. Engineering Manufacture*, 2002, **216**(12), 73–85.

9 **Chao, Y.** and **Qi, X.** Thermal and thermo-mechanical modeling of friction stir welding of aluminum alloy 6001-T6. *J. Mater. Processing Mfg Sci.*, 1998, **7**(10), 215–233.

10 **Deng, X.** and **Xu, S.** Solid mechanics simulation of friction stir welding process. *Trans. NAMR/SME*, 2001, **29**, 631–638.

11 **Xu, S., Deng, X., Raynolds, A. P.,** and **Seidel, T. U.** Finite element simulation of material flow in friction stir welding. *Sci. Technol. Weld. Joining*, 2001, **6**(3), 191–193.

12 **Dong, P., Lu, F., Hong, J. K.,** and **Cao, Z.** Coupled thermomechanical analysis of friction stir welding process using simplified models. *Sci. Technol. Weld. Joining*, 2001, **6**(5), 281–287.

13 **Chen, C. M.** and **Kovacevic, R.** Joining of aluminum to steel with a combination of solid state welding and fusion welding. *Intl J. Mach. Tools Mf.*, 2004, **44**, 1205–1214.

14 **Chen, C. M.** and **Kovacevic, R.** Thermomechanical modeling and force analysis of friction stir welding by finite element method. *Proc. Instn Mech. Engrs, Part C: J. Mechanical Engineering Science*, 2004, **218**, 509–519.

15 **Ulysse, P.** Three-directional modeling of the friction stir-welding process. *Int. J. Mach. Tools Mf.*, 2002, **42**, 1549–1557.

16 **Shi, Q.-Y., Dickerson, T.,** and **Shercliff, H. R.** Thermo-mechanical analyses of welding aluminum alloy with TIG and friction stir welding. In Proceedings of the ASM International Conference on *Trends in welding research*, 2002, pp. 247–252 (ASM International, Materials Park, Ohio).

17 **Shi, Q.-Y., Dickerson, T.,** and **Shercliff, H. R.** Thermo-mechanical FE modeling of friction stir welding of Al-2024 including tool loads. In Proceedings of the Fourth International Symposium on *Friction stir welding*, Park City, Utah, USA, May 2003 (TWI, Cambridge).

18 *ANSYS user's manual: elements*, Release 5.7, Vol. III (Swanson Analysis Systems, Inc., Canonsburg, Pennsylvania).

19 **Masubuchi, K.** *Analysis of welded structures*, 1980 (Pergamon, Oxford).

20 **Webster, P. J., Djapic Oosterkamp, L., Browne, P. A., Hughes, D. J., Kang, W. P., Withers, P. J.,** and **Vaughan, G. B. M.** Synchrotron X-ray residual strain scanning of a friction stir weld. *J. Strain Analysis*, 2000, **36**(1), 61–70.

21 **Wang, X. L., Feng, Z., David, S. A., Spooner, S.,** and **Hubbard, C. R.** Neutron diffraction study of residual stresses in friction stir welds. In Proceedings of the Sixth International Conference on *Residual stresses*, London, UK, 2000, pp. 1408–1415 (IOM Communications, London).

22 **Djapic Oosterkamp, L., Webster, P. J., Browne, P. A., Vaughan, G. B. M.,** and **Whiters, P. J.** Residual stress field in a friction stir welded aluminum extrusion. *Mater. Science Forum*, 2000, 247–249, 678–683.

APPENDIX 1

Notation

$[B]$	strain function matrix
c	heat capacity (kJ/kg °C)
$[D]$	displacement function matrix
F	volume force intensity (N/m^3)
k	conductivity (W/m °C)
$[M]$	stress function matrix
$p(T)$	pressure on the shoulder of the tool (N/m^2)
q	heat generation rate per unit volume (J/m^3 s)
$\dot{q}$	heat generation rate (J/s)
r	radius (m)
r_0	outer radius of the probe (m)
R_0	outer radius of the shoulder (m)
S	stress tensor (MPa)
T	temperature (°C)
U	displacement (m)
U_y	normal displacement (m)
V	tool traverse speed (m/s)
γ	acceleration (m/s^2)
ε	total strain tensor
ε^{e}	elastic strain
ε^{p}	plastic strain
ε^{t}	thermal strain
ρ	material density (kg/m^3)
ω	rotational speed of the shoulder (rev/s)